Epitaxial growth of honeycomb-like stanene on Au(111)

Wenhui Pang[1], Kazuki Nishino[1], Tsuyoshi Ogikubo[1], Masaaki Araidai[1,2,3],

Masashi Nakatake[4], Guy Le Lay[5], Junji Yuhara[1*]

[1] *Department of Energy Engineering, Nagoya University, Nagoya 464-8603, Japan*

[2] *Institute for Advanced Research, Nagoya University, Nagoya 464-8601, Japan*

[3] *Institute of Materials and Systems for Sustainability, Nagoya University, Nagoya 464-8601, Japan*

[4] *Aichi Synchrotron Radiation Center, Aichi Science & Technology Foundation, Seto, Aichi 489-0965, Japan*

[5] *Aix-Marseille Université, CNRS, PIIM UMR 7345, 13397 Marseille Cedex, France*

Abstract

Stanene, which is predicted to be a quantum spin Hall topological insulator with tunable topological state, seems to be the most promising candidate of the post-graphene elemental two-dimensional (2D) materials. Here, we prepared epitaxial honeycomb-like stanene on gold (111) substrates and investigated its superstructure by Low Energy Electron Diffraction and Scanning Tunneling Microscopy. Angle-Resolved PhotoEmission Spectroscopy was applied to explore the electronic structures, further confirmed by first principles calculations. The stanene-like sheet forms a nearly planar structure on the Au(111) surface with a "2×√3" superstructure in large surface areas. Core-level spectroscopy reveals that the stanene-like sheet lays almost directly on the Au(111) surface. This is consistent with DFT calculations of the atomic structure. A characteristic 2D band with parabolic dispersion is observed.

Keywords

Stanene; Epitaxial growth; Au(111); STM

*Corresponding author: Junji Yuhara (j-yuhara@energy.nagoya-u.ac.jp)

1. Introduction

The success of graphene has driven extensive attention to other two-dimensional (2D) materials, due to outstanding properties, such as topological insulating character [1], Quantum Spin Hall (QSH) effect [2,3], and enhanced thermoelectricity [4]. Unfortunately, however, most available materials with such properties are until now often based on multi-component materials with different sublattices or complex alloys. These are still challenging to fabricate in terms of large-scale production. Among various post-graphene elemental 2D materials [5], one of them, stanene, the tin-based analog, attracted special attention due to its Dirac cone-like energy dispersion and large spin-orbit strength, permitting to envision exciting emerging properties. Typically, it has been predicted that stanene with a large gap 2D QSH state can enable dissipationless electric conduction at room temperature (RT) [6–8]. Several theoretical and experimental efforts have been carried out on stanene [9–11], e.g., stanene with a 0.44 eV band gap, has been grown on InSb(111) recently [12].

The first realization of a highly buckled stanene-like overlayer has been achieved on a Bi_2Te_3 topological insulator substrate [13]. Then further researches have been devoted to exploring the distinct electronic properties of stanene formed on different substrates, such as semiconducting InSb(111), SiC(0001) and MoS_2 [11,14,15], semimetals Sb(111) [16], and metallic Ag(111) [17], Cu(111) [18]; for interesting reviews, see refs. 19 and 20. Searching for alternative substrate materials, recent theoretical works especially predicted interesting possibilities with the Au(111) surface [21], while density functional theory (DFT) calculations indicate that low-buckled stanene is more stable than highly buckled stanene [3].

A few groups have studied the growth of tin on gold (111) surfaces by different methods [22–27]. However, the experimental realization of stanene remains challenging. To the best of our knowledge planar honeycomb-like tin with a "$2\times\sqrt{3}$" superstructure on the Au(111) surface, as will be shown here, has never been reported; hence, we will describe its realization and properties in this paper.

This novel tin overlayer features a low-buckled lattice with eventually three Sn atoms per unit cell arranged in a honeycomb-like structure, as derived from scanning tunneling microscopy (STM), low-energy electron diffraction (LEED) and synchrotron radiation core-level spectroscopy (CLS), along with DFT calculations of the atomic geometry. The electronic properties were explored by angle-resolved photoemission spectroscopy (ARPES), and compared to DFT band structure calculations.

2. Experiment and calculations

We performed our experiments in two different ultra-high vacuum vessels. The first one at Nagoya University, is equipped with a LEED apparatus operating with a LaB_6 filament and a UHV Omicron STM-1 system. The second one used for the CLS and ARPES experiments, is at the Aichi synchrotron radiation center. It hosts a MCP-LEED system and a hemispherical analyzer with a 200 mm radius (MB Scientific AB A-1) and wide-angle electron lens. Both vessels consist of a preparation chamber and an analysis chamber with base pressure lower than 10^{-10} mbar.

After sputtering the Au(111) surfaces by 700 eV Ar^+ ions at RT, an annealing at around 600 °C was performed. Temperatures were monitored with a radiation thermometer and a type K thermocouple fixed on the base plate of the sample holder. After annealing, Auger electron spectroscopy (AES) was performed at RT to check for surface cleanliness. Then the LEED patterns showed sharp reconstruction spots of the well-known Au(111)22×√3 herringbone clean superstructure.

Tin was deposited onto the Au(111) surfaces at RT in either UHV vessel with a deposition rate of approximately 0.13 monolayer (ML) min^{-1} (the rate was measured by using a quartz crystal monitor). The atomic density of a Au(111) plane is 1.391×10^{15} atoms cm^{-2} ; we use this value to define 1 ML Sn coverage. The deposition rate had been calibrated by Rutherford backscattering spectroscopy (RBS); the methodology has been published in refs. 28 and 29. The amount of deposited Sn is 0.6 ML; errors are less than 10% in mentioned coverage ratios.

In each vessel, the LEED and STM observations were performed at RT. Sharp LEED patterns were obtained with 46-70 eV primary beam energies. All STM images were acquired with W tips. The CL and ARPES spectra were recorded at about 10 K, as the gold specimen was mounted on a liquid-helium-cooled cryostat with 4-axis pulse motor control.

The DFT calculations were performed by the QuantumATK [30], in which wave functions are expressed by the linear combination of pseudo atomic orbitals. The interactions between ionic core and valence electrons were described by ONCV-type pseudopotentials of the PseudoDojo project [31,32] and PBE-type exchange-correlation energy functional was also employed [33]. The lateral size of the Au(111) simulation cell was (a,b) = (5.768, 4.995) in unit of Å; periodic boundary conditions were imposed along both directions. In the c direction, one side of the Au(111) slab consisting of 14 atomic layers was coupled to the semi-infinite Au(111) electrode as the boundary condition by the Green's function technique [34], and the opposite side had a vacuum region of 15 Å. The atomic configuration except for three layers close to the electrode was relaxed until the forces acting on atoms became smaller than 10 meV/Å. The cutoff energy for space discretization was taken to be 2721.14 eV. The Brillouin zone of the unit cell was sampled with a 5×6×1 Γ-center k-point grid.

3. Results and discussion

In order to study the growth of tin on the Au(111) surface, at first LEED and STM observations have been carried out. Fig. 1(a) and (b) show the LEED pattern and STM images of the well characterized Au(111)22×√3 herringbone reconstruction [35]. Terraces are separated by atomic steps 0.23 nm in height, as shown by the AB profile in Fig. 1 (b) and Fig 1 (f).

The LEED pattern and the large scale STM image (100 nm×100 nm) of the 0.60 Sn ML on the Au(111) surface are displayed in the Fig. 1 (c) and (d). After deposition, the LEED patterns exhibit the characteristic diffraction pattern of the "2×√3" superstructure,

which is simulated in Fig. 1 (e) with three symmetry equivalent domains. Along the $[1\bar{1}0]$ and $[11\bar{2}]$ directions the new lattice constants $\mathbf{b}_1$ and $\mathbf{b}_2$ are expanded/reduced with respect to commensurate $2\mathbf{a}_1$ and $\sqrt{3}\mathbf{a}_2$ values of the unreconstructed Au(111)1×1 surface, that is $|\mathbf{b}_1| = 1.1\times\sqrt{3}|\mathbf{a}_1|$ and $|\mathbf{b}_2| = 0.95\times 2|\mathbf{a}_2|$, the superstructure matrix being $\begin{bmatrix} 1.9 & 0.0 \\ 1.1 & 2.2 \end{bmatrix}$. This is why we name the superstructure as "2×√3", since it is in reality incommensurate. This may be related to the uniaxial compression of the gold surface atoms along the $[1\bar{1}0]$ direction [35].

In Fig. 1 (d), the smooth terraces no longer show any signature of the herringbone reconstruction and no 3D islands are observed. Locally, bare Au(111) is recognized as black holes. These terraces are separated by steps with a uniform height of 0.23 nm as shown in Fig. 1 (g), indicating a Au(111) step below the tin overlayer. Clearly the Sn atoms form an adlayer wetting the Au(111) surface; the overlayer film is uniform over hundred nanometers with just some second layer patches, as displayed in Fig. 1 (h).

The high-resolution STM image displayed in Fig. 2 (a) reveals the atomic arrangement of the "2×√3" superstructure. It points to two different local arrangements, namely chain-like within the yellow rectangles and honeycomb-like (hexagonal motifs are aligned only in one direction) within the black squares, as illustrated in Fig 2 (b) and (e), respectively, with possibly three equivalent orientations. In the black square areas, the protrusions appear denser than in the yellow rectangle ones, where they look like zigzag chains.

Assuming commensurate (2×√3) cells, representing approximants, we propose two atomic models differing in tin coverage ratios, respectively 0.5 ML and 0.75 ML, as shown in Fig 2 (b), (c), (e) and (f). This allows us to perform DFT calculations of the relaxed structures -where all Sn atoms have just a slight preference (by 0.03/0.02 eV) for *hcp* hollow sites compared to *fcc* ones-, and to simulate their corresponding STM images (Fig. 2 (d) and (g)). As clearly seen, they show zigzag chains with two Sn atoms, labelled 1 and 2 per (2×√3) cell, having the same environment, and a honeycomb-like

structure with three Sn atoms labelled 1, 2 and 3 per cell, where atom 2 has a different environment, in excellent agreement with the STM observations. As both zigzag chain-like and honeycomb-like arrangements are observed, indicating local Sn adatom density fluctuations at the 0.6 ML coverage, clearly both structures are energetically stable, which is confirmed in our DFT calculations where the difference is less than 0.05 eV.

As shown in Fig. 3, we further performed high-resolution synchrotron radiation core-level (CL) spectroscopy of the shallow Sn 4d and Au 4*f* CL's in highly surface sensitive conditions. A spectrum recorded from the clean Au(111) surface fitted with two components (bulk: B at 84.02 eV binding energy (BE) and surface: S at 83.69 eV BE ones), in excellent agreement with the literature [36]) is shown in Fig. 3 (a). After the deposition of 0.6 ML Sn giving the "2×√3" superstructure, the corresponding Au $4f_{7/2}$ photoemission spectrum is presented in Fig. 3 (b). The S surface component has vanished, but new components, located at the higher binding energy side of the bulk component, have appeared. There are three components labelled C1, C2 and C3 at 84.29, 84.57 and 84.78 eV BEs, respectively. The bulk component B has markedly decreased, which is the expected behavior for a substrate core-level peak. Component C3 may be related to Au atoms that diffuse through the Sn layer forming the Au-Sn alloy [26]. We relate components C1 and C2 to the interface top Au(111) layer beneath Sn atoms, either in the chain-like or the honeycomb-like local arrangements.

As for the corresponding Sn 4*d* broad spectrum, displayed in Fig. 3 (c), we fit it with three distinct components, S1, S2, and S3, respectively at 24.31 (Sn $4d_{5/2}$), 24.01 and 24.50 eV BEs. The S3 component is of comparable intensity and appears at the same binding energy as for the Au-Sn alloy investigated in ref. 26, hence, it is in correspondence with C3 discussed above. The main component S2 is about twice the intensity of S1, indicating high and low Sn coverages, respectively. Therefore, we relate components S1 and S2 to the chain-like and the honeycomb-like local arrangements, respectively. This is in correspondence to the previous C1 and C2 Au $4f_{7/2}$ components

in the interface region.

We have further investigated the electronic band structure of the "2×√3" phase by ARPES measurements at a photon energy of 70 eV. The corresponding data are shown in Fig. 4. A scheme of the Au(111) and "2×√3" surface Brillouin zones is shown in Fig 4 (a). One notices that because of the expansion and compression mentioned above, the "2×√3" surface Brillouin zone is nearly a square, that is the $\bar{\Gamma}\bar{X}_{Sn}$ and $\bar{\Gamma}\bar{Y}_{Sn}$ distances are practically the same. The clean Au(111) surface exhibits the well-known Rashba spin splitting of the Shockley surface-state (S) around the $\bar{\Gamma}$ point, shown in Fig. 4 (b). With 0.6 Sn ML (S) has vanished, and a new parabolic surface electronic band is observed in Fig. 4 (c) and (d). We note that no signature of a Au-Sn alloy, i.e., typical Λ-shape bands around the Γ point, is present [25]. The effective mass m^* is calculated to be $0.41m_e$, where m_e is the electron rest mass, which is significantly higher than for that of the bare Au(111) Shockley surface state ($0.28m_e$). The Fermi velocity is estimated to be $1.4\times10_6$ m/s.

We have compared these experimental results to DFT calculations for the two commensurate (2×√3) approximant phases in Fig. 5. The surface band structure of the clean unreconstructed Au(111)1×1 surface is displayed in Fig. 5 (a) in the range corresponding to $\bar{X}_{Sn}$-$\bar{\Gamma}$-$\bar{X}_{Sn}$, revealing the (S) state, but significantly upward shifted. Fig. 5 (b) and (c) show the calculated dispersions along $\bar{X}_{Sn}$-$\bar{\Gamma}$-$\bar{X}_{Sn}$ for the Sn related bands of the (2×√3) phases at 0.5 and 0.75 Sn ML, respectively. However, there is no clear correspondence with the experimental dispersion in Fig. 4 (c), except possibly for the calculation shown in Fig. 5 (c) for the 0.75 ML coverage, i.e., for the honeycomb-like structure, or, in other words, the stanene-like structure, if we consider a likely up-shift. Hence, the stanene-like structure is more favorable in our experimental conditions, although, indeed, the DFT calculations for the commensurate (2×√3) approximant phase are just indicative.

Both experimental and theoretical parabolic dispersions clearly differ from the cone-like one expected for free-standing stanene, which is no surprise since, for one, the

stanene-like Sn overlayer is not purely honeycomb, and, for two, is interacting with the Au(111) substrate. However, we stress that the structural flatness of the stanene-like phase is likely to drive a large QSH effect, possibly even at RT [16].

4. Conclusion

In conclusion, the tin sheet forms a nearly planar structure on the Au(111) surface with a "2×√3" superstructure in large surface areas, identified by LEED patterns and STM images. In addition, based on experimental results, we proposed zigzag chain and honeycomb-like structures characterized by STM observations and DFT calculations. Meanwhile, the core-level spectra of Sn deposited onto the Au(111) surface reveal that a structurally flat stanene-like sheet lays almost directly on Au(111) surface. Both experimental and theoretical band structures favor a stanene-like honeycomb structure with three Sn atoms per unit cell.

Acknowledgments

The authors are grateful to Nagoya University Synchrotron Radiation Research Center for financial support for ARPES measurements, which were conducted at BL7U of Aichi Synchrotron Radiation Center, Aichi Science & Technology Foundation. JY acknowledges financial support from Murata Science Foundation in 2019. GLL acknowledges support from Nagoya University thanks to an "Eminent Foreign Scientist" Invitation Award in 2015-2016 and 2019-2020, as well as an Invitational Fellowship for Research in Japan by the Japan Society for the Promotion of Science (JSPS) in 2017. M.A. is partly supported by JSPS KAKENHI Grant Number 19H04541. The computation in this work has been done in part using the facilities at the Information Technology Center, Nagoya University.

References

[1] D. Pesin, A.H. MacDonald, Spintronics and pseudospintronics in graphene and topological insulators, Nature Mater. 11 (2012) 409–416. https://doi.org/10.1038/nmat3305.

[2] C.L. Kane, E.J. Mele, Quantum Spin Hall Effect in Graphene, Phys. Rev. Lett. 95 (2005) 226801. https://doi.org/10.1103/PhysRevLett.95.226801.

[3] Y. Xu, B. Yan, H.-J. Zhang, J. Wang, G. Xu, P. Tang, W. Duan, S.-C. Zhang, Large-Gap Quantum Spin Hall Insulators in Tin Films, Phys. Rev. Lett. 111 (2013) 136804. https://doi.org/10.1103/PhysRevLett.111.136804.

[4] Y. Ouyang, J. Guo, A theoretical study on thermoelectric properties of graphene nanoribbons, Appl. Phys. Lett. 94 (2009) 263107. https://doi.org/10.1063/1.3171933.

[5] J. Yuhara, B. He, N. Matsunami, M. Nakatake, G. Le Lay, Graphene's Latest Cousin: Plumbene Epitaxial Growth on a "Nano WaterCube", Adv. Mater. 31 (2019) 1901017. https://doi.org/10.1002/adma.201901017.

[6] M. Ezawa, Monolayer Topological Insulators: Silicene, Germanene, and Stanene, J. Phys. Soc. Jpn. 84 (2015) 121003. https://doi.org/10.7566/JPSJ.84.121003.

[7] Z. Ni, E. Minamitani, Y. Ando, S. Watanabe, Germanene and stanene on two-dimensional substrates: Dirac cone and Z 2 invariant, Phys. Rev. B. 96 (2017) 075427. https://doi.org/10.1103/PhysRevB.96.075427.

[8] S. Rachel, M. Ezawa, Giant magnetoresistance and perfect spin filter in silicene, germanene, and stanene, Phys. Rev. B. 89 (2014) 195303. https://doi.org/10.1103/PhysRevB.89.195303.

[9] J.-C. Rojas-Sánchez, S. Oyarzún, Y. Fu, A. Marty, C. Vergnaud, S. Gambarelli, L. Vila, M. Jamet, Y. Ohtsubo, A. Taleb-Ibrahimi, P. Le Fèvre, F. Bertran, N. Reyren, J.-M. George, A. Fert, Spin to Charge Conversion at Room Temperature by Spin Pumping into a New Type of Topological Insulator: α -Sn Films, Phys. Rev. Lett. 116 (2016) 096602. https://doi.org/10.1103/PhysRevLett.116.096602.

[10] B. Mortazavi, O. Rahaman, M. Makaremi, A. Dianat, G. Cuniberti, T. Rabczuk, First-principles investigation of mechanical properties of silicene, germanene and stanene, Physica E: Low-Dimensional Systems and Nanostructures. 87 (2017) 228–232. https://doi.org/10.1016/j.physe.2016.10.047.

[11] X. Zheng, J.-F. Zhang, B. Tong, R.-R. Du, Epitaxial growth and electronic properties of few-layer stanene on InSb (111), 2D Mater. 7 (2019) 011001. https://doi.org/10.1088/2053-1583/ab42b9.

[12] C.-Z. Xu, Y.-H. Chan, P. Chen, X. Wang, D. Flötotto, J.A. Hlevyack, G. Bian, S.-K. Mo, M.-Y. Chou, T.-C. Chiang, Gapped electronic structure of epitaxial stanene on InSb(111), Phys. Rev. B. 97 (2018) 035122. https://doi.org/10.1103/PhysRevB.97.035122.

[13] F. Zhu, W. Chen, Y. Xu, C. Gao, D. Guan, C. Liu, D. Qian, S.-C. Zhang, J. Jia, Epitaxial growth of two-dimensional stanene, Nature Mater. 14 (2015) 1020–1025. https://doi.org/10.1038/nmat4384.

[14] P. Li, Stanene on a SiC(0001) surface: a candidate for realizing quantum anomalous Hall effect, Phys. Chem. Chem. Phys. 21 (2019) 11150–11157. https://doi.org/10.1039/C9CP01509D.
[15] K.-C. Chen, L.-M. Lee, H.-A. Chen, H. Sun, C.-L. Wu, H.-A. Chen, K.-B. Lin, Y.-C. Tseng, C.-C. Kaun, C.-W. Pao, S.-Y. Lin, Multi-layer elemental 2D materials: antimonene, germanene and stanene grown directly on molybdenum disulfides, Semicond. Sci. Technol. 34 (2019) 105020. https://doi.org/10.1088/1361-6641/ab3c8a.
[16] J. Gou, L. Kong, H. Li, Q. Zhong, W. Li, P. Cheng, L. Chen, K. Wu, Strain-induced band engineering in monolayer stanene on Sb(111), Phys. Rev. Materials. 1 (2017) 054004. https://doi.org/10.1103/PhysRevMaterials.1.054004.
[17] J. Yuhara, Y. Fujii, K. Nishino, N. Isobe, M. Nakatake, L. Xian, A. Rubio, G. Le Lay, Large area planar stanene epitaxially grown on Ag(111), 2D Mater. 5 (2018) 025002. https://doi.org/10.1088/2053-1583/aa9ea0.
[18] R. Ahmed, T. Nakagawa, S. Mizuno, Structure determination of ultra-flat stanene on Cu(111) using low energy electron diffraction, Surface Science. 691 (2020) 121498. https://doi.org/10.1016/j.susc.2019.121498.
[19] P. Vishnoi, K. Pramoda, C.N.R. Rao, 2D Elemental Nanomaterials Beyond Graphene, ChemNanoMat. 5 (2019) 1062–1091. https://doi.org/10.1002/cnma.201900176.
[20] J. Lyu, S. Zhang, C. Zhang, P. Wang, Stanene: A Promising Material for New Electronic and Spintronic Applications, ANNALEN DER PHYSIK. 531 (2019) 1900017. https://doi.org/10.1002/andp.201900017.
[21] S. Nigam, S. Gupta, D. Banyai, R. Pandey, C. Majumder, Evidence of a graphene-like Sn-sheet on a Au(111) substrate: electronic structure and transport properties from first principles calculations, Phys. Chem. Chem. Phys. 17 (2015) 6705–6712. https://doi.org/10.1039/C4CP04861J.
[22] M.-G. Barthès, C. Pariset, A low energy electron diffraction-Auger electron spectroscopy study of alloy formation during the adsorption of tin on (100) and (111) Au, Thin Solid Films. 77 (1981) 305–312. https://doi.org/10.1016/0040-6090(81)90322-9.
[23] M. Maniraj, B. Stadtmüller, D. Jungkenn, M. Düvel, S. Emmerich, W. Shi, J. Stöckl, L. Lyu, J. Kollamana, Z. Wei, A. Jurenkow, S. Jakobs, B. Yan, S. Steil, M. Cinchetti, S. Mathias, M. Aeschlimann, A case study for the formation of stanene on a metal surface, Commun Phys. 2 (2019) 12. https://doi.org/10.1038/s42005-019-0111-2.
[24] Y. Liu, N. Gao, J. Zhuang, C. Liu, J. Wang, W. Hao, S.X. Dou, J. Zhao, Y. Du, Realization of strained stanene by interface engineering, J. Phys. Chem. Lett. 10 (2019) 1558–1565. https://doi.org/10.1021/acs.jpclett.9b00348.
[25] P. Sadhukhan, D. Pandey, V.K. Singh, S. Sarkar, A. Rai, K. Bhattacharya, A. Chakrabarti, S. Roy Barman, Electronic structure and morphology of thin surface alloy layers formed by deposition of Sn on Au(111), Applied Surface Science. 506

(2020) 144606. https://doi.org/10.1016/j.apsusc.2019.144606.
[26] P. Sadhukhan, S. Barman, T. Roy, V.K. Singh, S. Sarkar, A. Chakrabarti, S.R. Barman, Electronic structure of Au-Sn compounds grown on Au(111), Phys. Rev. B. 100 (2019) 235404. https://doi.org/10.1103/PhysRevB.100.235404.
[27] D. Zhou, N. Si, B. Jiang, X. Song, H. Huang, Q. Ji, T. Niu, Interfacial effects on the growth of atomically thin film: Group VA elements on Au(111), Adv. Mater. Interfaces. 6 (2019) 1901050. https://doi.org/10.1002/admi.201901050.
[28] J. Yuhara, M. Inoue, K. Morita, Phase transition of the Si(111)–Au surface from √3×√3 to 5×1 structure studied by means of the low-energy electron diffraction, Auger electron spectroscopy, and Rutherford backscattering spectroscopy techniques, Journal of Vacuum Science & Technology A. 10 (1992) 334–338. https://doi.org/10.1116/1.578053.
[29] J. Yuhara, K. Morita, J. Falta, B.H. Müller, M. Horn-von Hoegen, Characterization of Ge δ-doped Si(111) with RBS channeling, Surface and Interface Analysis. 31 (2001) 754–760. https://doi.org/10.1002/sia.1106.
[30] https://www.synopsys.com/silicon/quantumatk.html
[31] M.J. van Setten, M. Giantomassi, E. Bousquet, M.J. Verstraete, D.R. Hamann, X. Gonze, G.-M. Rignanese, The PseudoDojo: Training and grading a 85 element optimized norm-conserving pseudopotential table, Computer Physics Communications. 226 (2018) 39–54. https://doi.org/10.1016/j.cpc.2018.01.012.
[32] http://www.pseudo-dojo.org/
[33] J.P. Perdew, K. Burke, M. Ernzerhof, Generalized Gradient Approximation Made Simple, Phys. Rev. Lett. 77 (1996) 3865–3868. https://doi.org/10.1103/PhysRevLett.77.3865.
[34] M. Brandbyge, J.-L. Mozos, P. Ordejón, J. Taylor, K. Stokbro, Density-functional method for nonequilibrium electron transport, Phys. Rev. B. 65 (2002) 165401. https://doi.org/10.1103/PhysRevB.65.165401.
[35] J.V. Barth, H. Brune, G. Ertl, R.J. Behm, Scanning tunneling microscopy observations on the reconstructed Au(111) surface: Atomic structure, long-range superstructure, rotational domains, and surface defects, Phys. Rev. B. 42 (1990) 9307–9318. https://doi.org/10.1103/PhysRevB.42.9307.
[36] K. Heister, M. Zharnikov, M. Grunze, L.S.O. Johansson, Adsorption of Alkanethiols and Biphenylthiols on Au and Ag Substrates: A High-Resolution X-ray photoelectron spectroscopy study, J. Phys. Chem. B. 105 (2001) 4058–4061. https://doi.org/10.1021/jp010127q.

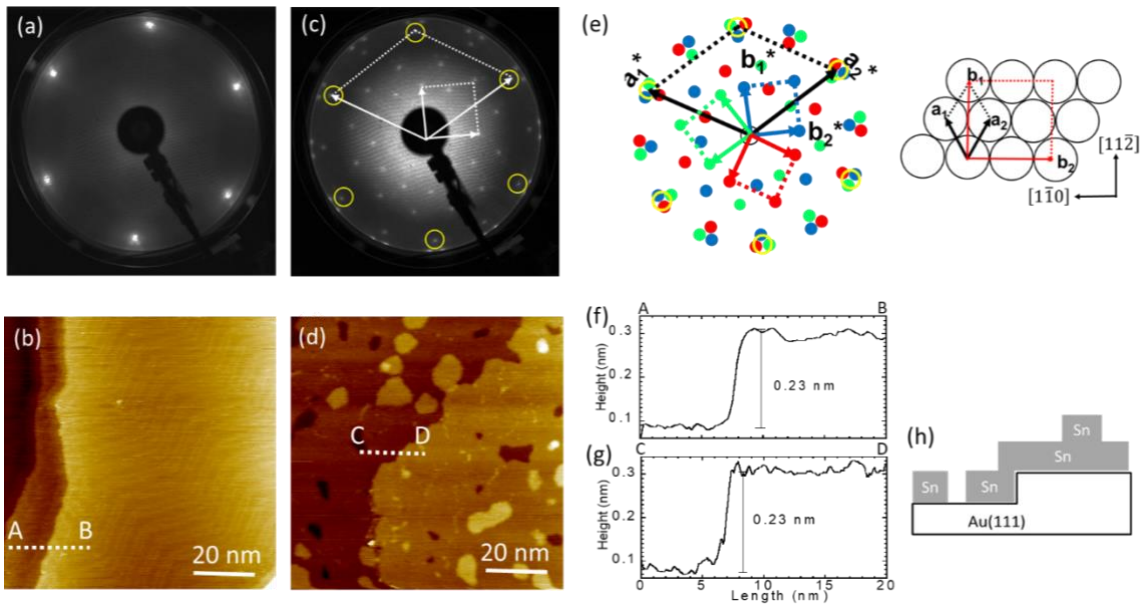

Fig. 1 (a) LEED pattern of the pristine Au(111) surface (55 eV). (b) large-scale STM image of the bare Au(111) surface showing the herringbone superstructure (Us = 1.0 V, I = 0.2 A). (c) and (d) LEED pattern (55 eV) and the large-scale STM image (Us = 1.0 V, I = 0.2 nA) of 0.6 ML Sn deposited onto the Au(111) surface at RT. (e) Simulated LEED pattern of the "2×√3" superstructure. (f) and (g) Sectional profiles along the A-B and C-D lines in (b) and (d). (h) Growth model of tin on the Au(111) surface.

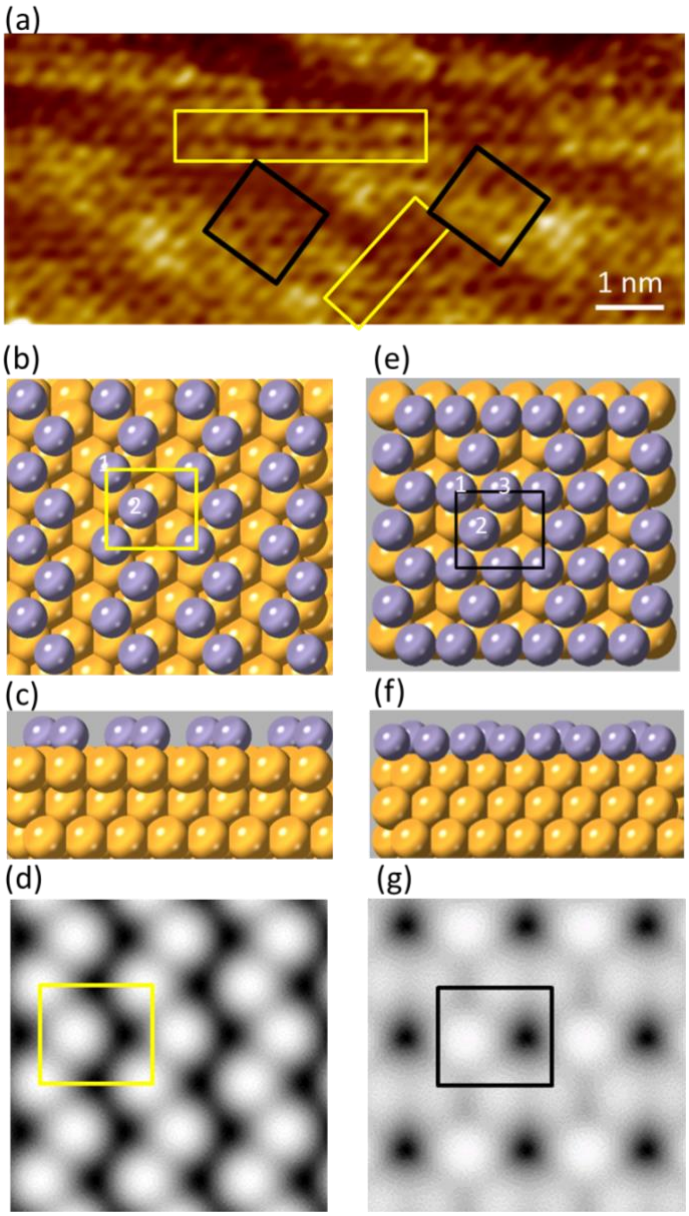

Fig. 2 (a) High-resolution STM image of the Sn covered Au(111) surface (0.6 ML; Us = 0.3 V, I = 0.2 nA). (b) and (c) Top and side views of the zigzag chain-like (2×√3) approximant structure. (e) and (f) Top and side views of the honeycomb-like (2×√3) approximant structure. Yellow and gray balls denote Au and Sn atoms, respectively. Yellow and black squares indicate the (2×√3) unit cell. (d) and (g) are the simulated STM images for the zigzag chain-like and honeycomb-like structures, respectively.

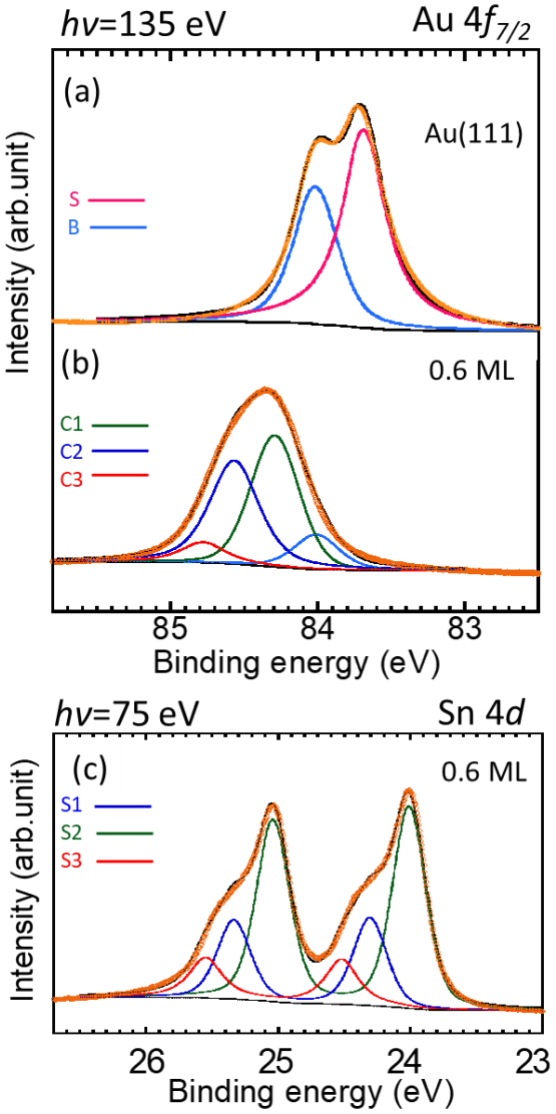

Fig. 3 The core level spectra of Au 4*f* and Sn 4*d* measured at 10 K and taken at hν = 135 eV and 75 eV, respectively. (a) Au $4f_{7/2}$ for a clean bare Au(111) single crystal, (b) and (c) Au $4f_{7/2}$ and Sn 4*d* of stanene on Au(111) surface. The orange circle line is the fit line, and the black line is the experiment's data.

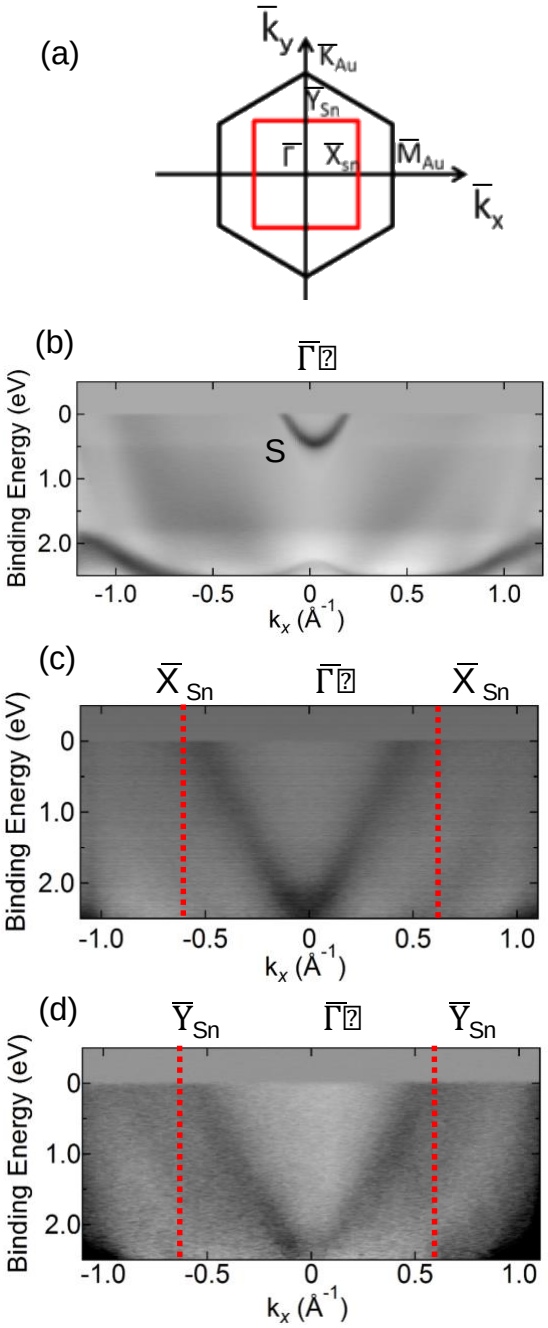

Fig. 4 ARPES dispersion at *hv* = 70 eV, measured at 10 K. (a) Scheme of the Au(111) surface Brillouin zone in black and of the "2×√3" Sn phase in red. (b) Shockley surface state of the clean Au(111) surface along the $\bar{M}_{Au}$-$\bar{\Gamma}$-$\bar{M}_{Au}$ direction. (c) and (d) electronic band structures of the "2×√3" stanene-like phase on the Au(111), measured along the $\bar{M}_{Au}$– $\bar{X}_{Sn}$-$\bar{\Gamma}$- $\bar{X}_{Sn}$–$\bar{M}_{Au}$ and $\bar{K}_{Au}$–$\bar{Y}_{Sn}$-$\bar{\Gamma}$-$\bar{Y}_{Sn}$–$\bar{K}_{Au}$ directions.

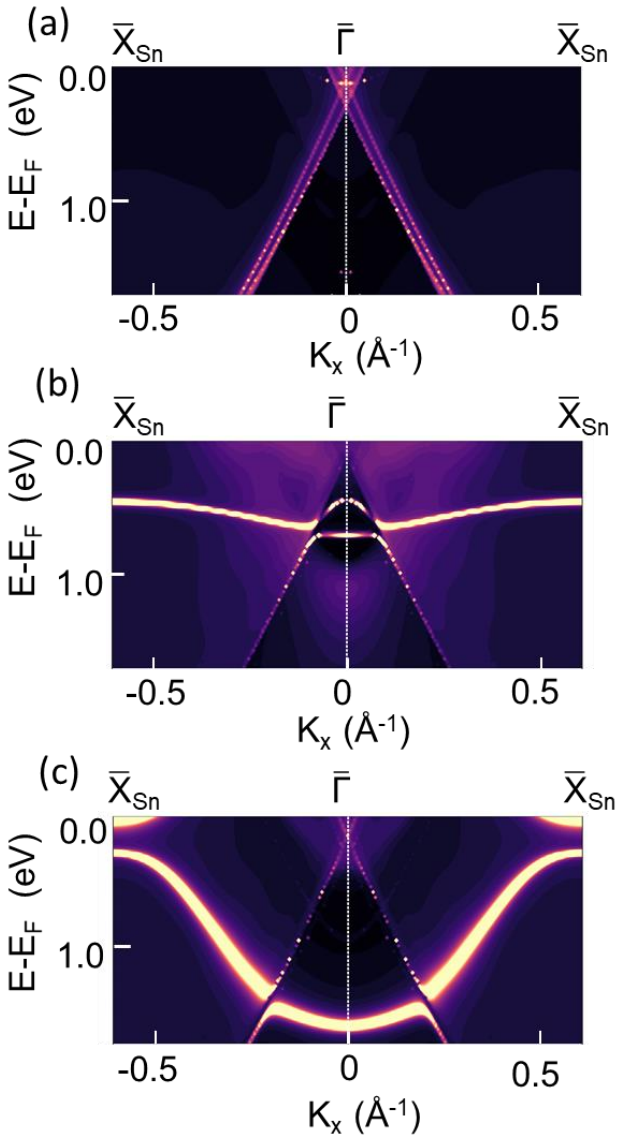

Fig. 5 (a) The calculated surface band structures along the $\bar{X}_{Sn}$-$\bar{\Gamma}$-$\bar{X}_{Sn}$ interval for bare Au(111)1×1 surface. (b) The Sn-related band structure for the chain-like phase at 0.5 ML Sn coverage. (c) The Sn-related band structure for the stanene-like phase at 0.75 ML Sn coverage.